ADVANCES IN ATMOSPHERIC SCIENCES, VOL. 36, FEBRUARY 2019, 189–205

• **Original Paper** •

Satellite-based Observational Study of the Tibetan Plateau Vortex: Features of Deep Convective Cloud Tops

Yi-Xuan SHOU*[1], Feng LU[1], Hui LIU[1], Peng CUI[1], Shaowen SHOU[2], and Jian LIU[1]

[1]*Key Laboratory of Radiometric Calibration and Validation for Environmental Satellites, China Meteorological Administration (LRCVES/CMA) National Satellite Meteorological Center, Beijing* 100081*, China*

[2]*Key Laboratory of Meteorological Disasters, Nanjing University of Information Sciences and Technology, Nanjing* 210044*, China*

(Received 26 February 2018; revised 12 July 2018; accepted 20 August 2018)

ABSTRACT

In this study, an east-moving Tibetan Plateau vortex (TPV) is analyzed by using the ERA-5 reanalysis and multi-source satellite data, including FengYun-2E, Aqua/MODIS and CALIPSO. The objective is to demonstrate: (i) the usefulness of multi-spectral satellite observations in understanding the evolution of a TPV and the associated rainfall, and (ii) the potential significance of cloud-top quantitative information in improving Southwest China weather forecasts. Results in this study show that the heavy rainfall is caused by the coupling of an east-moving TPV and some low-level weather systems [a Plateau shear line and a Southwest Vortex (SWV)], wherein the TPV is a key component. During the TPV's life cycle, the rainfall and vortex intensity maintain a significant positive correlation with the convective cloud-top fraction and height within a 2.5° radius away from its center. Moreover, its growth is found to be quite sensitive to the cloud phases and particle sizes. In the mature stage when the TPV is coupled with an SWV, an increase of small ice crystal particles and appearance of ring- and U/V-shaped cold cloud-top structures can be seen as the signature of a stronger convection and rainfall enhancement within the TPV. A tropopause folding caused by ageostrophic flows at the upper level may be a key factor in the formation of ring-shaped and U/V-shaped cloud-top structures. Based on these results, we believe that the supplementary quantitative information of an east-moving TPV cloud top collected by multi-spectral satellite observations could help to improve Southwest China short-range/nowcasting weather forecasts.

Key words: Tibetan Plateau vortex, multi-spectral satellite observations, short-range/nowcasting weather forecasts, cold U/V-shaped cloud top, tropopause folding

Citation: Shou, Y.-X., F. Lu, H. Liu, P. Cui, S. W. Shou, and J. Liu, 2019: Satellite-based observational study of the Tibetan Plateau Vortex: Features of deep convective cloud tops. *Adv. Atmos. Sci.*, **36**(2), 189–205, https://doi.org/10.1007/s00376-018-8049-y.

1. Introduction

Southwestern China is located at the border of middle and low latitude zones on the east of the Tibetan Plateau, wherein 81% of the area is covered by many north–south oriented mountains and rivers. Due to its extremely complicated topography and unique geographical position, the climate in this region is distinctive and the weather is changeable and complex. Therefore, much attention has been paid to the weather and climate issues over Southwest China, stretching back a long time (Ye and Gao, 1979; Lu, 1986; Zhu et al., 2000).

The Tibetan Plateau Vortex (TPV) is one of the typical circulation and weather systems in Southwest China. Due to its impact on severe weather, it has been the object of study since it was discovered (Tao, 1980; Chen, 1988; Chen et al., 2003; Wang et al., 2007; Li et al., 2012). A TPV is generally defined as a meso-α-scale vortex with a horizontal scale of 400–500 km and generated at 500 hPa within the Tibetan Plateau (27°–40°N, 70°–110°E) (Luo, 1992). Under favorable synoptic conditions, some TPVs can move out from the Plateau and couple with some other meso-/micro-scale weather systems to cause heavy rainfall and thunderstorm events in downstream areas (Chen et al., 2004; Zhao and Wang, 2010; Chen and Li, 2014; Fu et al., 2015; Cheng et al., 2016; Yu and Gao, 2017; Zhou et al., 2017). Recently, results of some climatology studies have indicated an increase in the frequency of TPVs in the context of global warming (Li et al., 2014; Huang et al., 2015; Li et al., 2017), and thus they may have a larger impact on downstream areas, such as the Sichuan Basin, Yangtze River Basin, and even North China. Therefore, the demand for a higher prediction accuracy of TPVs arises.

* Corresponding author: Yi-Xuan SHOU
Email: shouyx@cma.gov.cn

As a result of uncertainties in the initial conditions along with the "model error", the prediction of TPVs and their associated rainstorms is always a challenge for operational forecasters in China. On the one hand, such uncertainties and errors are caused by the difficulties in gathering the meteorological data in the Plateau and its vicinity. On the other hand, they are the result of insufficient knowledge about the evolutionary characteristics of the systems that operate in this unique landscape of the Plateau, as well as the complicated impact factors at play.

Before the 1990s, most studies on TPVs were made based on the data from several sounding stations spread over Southwest China. The average distance among them was about 500 km and the temporal resolution was 12 hours. With such a coarse resolution, some of the finer-scale structures and evolutionary features of TPVs were undoubtedly missed. For this reason, in predictions and analyses of TPVs nowadays, more attention is paid to remote sensing data, due to its capacity in providing information of higher spatiotemporal resolution from multiple angles.

As an atmospheric remote sensing tool, satellites have a wider field of view and are almost unaffected by geographical location compared with weather radar. Therefore, their data can be applied more extensively. Unlike conventional observations, such as radiosonde, rawinsonde etc., the sensors onboard satellites are designed to receive the electromagnetic radiation reflected or emitted by clouds, precipitation particles or raindrops (Xu et al., 2000). As one of the core objects in satellite observations, cloud is known to be a good indicator for the evolution of weather systems. Thus, it has been used in weather analyses and forecasts in many countries (Bedka and Mecikalski, 2005; Mecikalski et al., 2007, 2016; Siewert et al., 2010; Setvák et al., 2010, 2013). To date, many efforts have been made to obtain quantitative cloud information that can indicate the evolution of mesoscale convective systems (MCSs). Both Schmetz et al. (1997) and Kurino (1997) proposed methods for estimating convection intensity based on the radiation differences between channels of the Meteosat and GMS-5 geostationary satellites. Machado et al. (1998) studied the morphology and radiative properties of MCSs over the Americas based on year-long GOES-7 satellite observations. They found that an MCS's lifetime is directly correlated to the sizes of the convective clouds, and the size and lifetime stage can be reflected by the mean cloud radiation around it. Thus, the aforementioned information can be used in predicting the changes in MCSs. Recently, with developments in the spectral and spatiotemporal resolutions of satellites, more information can be obtained and used in severe weather monitoring and forecasting. Through GOES satellite data, Mecikalski et al. (2008) found the cloud-top cooling rate, the evolution of the brightness temperature difference (BTD) between 6.5 and 10.7 μm, as well as that between 13.3 and 10.7 μm, can be applied in predicting the convective initiation. Based on multispectral satellite data, Setvák et al. (2013) revealed that some small scale structures at the top of convective clouds, such as "U/V"-shaped structures, are related to the convection intensity.

In the past several decades, studies of TPVs based on satellite observations have mainly focused on two aspects: one is the cloud distribution patterns, including the overall morphological features and radiative properties in a single spectral channel; and the other is the characteristics of the microphysical three-dimensional structure (Xiang et al., 2013; Yu et al., 2014; Jiang et al., 2015; Jiang and Li, 2015). For example, Yu (2002) and Yu and He (2003) used the water vapor (WV) image data gathered from the GMS-5 geostationary satellite to study a TPV, and found the vortex in the WV images formed earlier than the TPV on the weather map. In addition, they suggested using areas with brightness temperature (TBB) of 223 K in WV channel images as an indicator for the activities in TPVs to monitor a TPV's development. Huang and Li (2009) once investigated the TPV cloud distribution features by FengYun-2C and MTSAT satellite observations, and found that a TPV reaches the mature stage when it has a similar eye and warm-core structure to tropical cyclone–like vortices. Xiang et al. (2013) studied the microphysical structures of a TPV cloud cluster based on the precipitation radar data of the TRMM satellite. They pointed out that the TPV cloud top can grow up to 15 km, and the increase in particle sizes at the midlow level is conducive to the increase in precipitation. All in all, although our understanding of the mechanisms and structures of TPVs has to some extent improved by taking advantage of satellite observations, the usage of satellite observations in TPV analysis and prediction is still limited when compared with other disastrous mesoscale weather systems, such as tropical cyclones, which resemble TPVs the most. With respect to the advantages of satellites, more features and quantitative information at the top of TPV storm clouds should be found and recognized from the spectral space.

Therefore, a TPV in a severe rainstorm over the mid-west of Sichuan Province during 8–11 July 2013 is taken as an example in this study to discuss (i) the usefulness of multispectral satellite observations in understanding the TPV and the associated rainfall; and (ii) the potential significance of quantitative information at the cloud top in improving short-range or nowcasting weather forecasts over Southwest China. These objectives are to be achieved by analyzing reanalysis data and multi-spectral satellite observational data, including the data from polar-orbiting and geostationary orbit satellites.

Following this introduction, section 2 introduces the selected case and data used in this study. Section 3 presents the evolutionary characteristics of the cloud top that are concerned with the evolution of the TPV and its associated precipitation. Section 4 discusses the possible mechanisms for forming a "U/V" cloud-top structure. A summary and concluding remarks are given in section 5.

2. Case overview and data description

2.1. *Case overview*

In July 2013, five extreme and sustained rainfall events occurred over Southwest China. Among them, only the pro-

cess during 8–11 July 2013 was not to a certain extent impacted by a landfalling typhoon. However, the intensity of the precipitation during 8–11 July 2013 (hereafter referred to as the "7.8" rainfall) was the strongest during that period (Sun et al., 2015). Besides, according to observations, over 14% of the Chinese mainland had an accumulated rainfall above 50 mm in the "7.8" rainfall, and it even reached above 700 mm in some regions (Fig. 1a). The daily accumulated rainfall at Dujiangyan station of Sichuan Province, the center of the "7.8" rainfall, was over 292 mm during 8–9 July, which was beyond the historical extreme for this station in the first 10 days of July (the last extreme value was 233 mm in July 2011).

As shown by the variation of the hourly rainfall over the precipitation center (Fig. 1b), the whole process can be divided into two phases: one is during 1100 LST 8 July to 1500 LST 9 July (LST = UTC + 8 h), with an extreme precipitation rate of 130 mm h^{-1} around 0200–0300 LST 9 July; and the other is during 1600 LST 9 July to 0000 LST 11 July, with an extreme of 60 mm h^{-1} during 0200–0300 LST 10 July. Comparatively, the former stage was more intense than the latter.

Figure 2 shows the ERA-5 geopotential height fields at 500 hPa superimposed by jet streams at 200 hPa and 850 hPa at 2000 LST on 8 and 9 July 2013. We can see that during the whole process, the middle and low latitude zones were controlled by the monsoon low, and the shortwave activities were frequent in the southern trough in Southwest China (Fig. 2). The subtropical high ridge line stayed relatively stable at 30°N, but extended to the west and shrank in the east. At 2000 LST 8 July, when the first stage of the precipitation enhanced, the west-extending point of the subtropical high

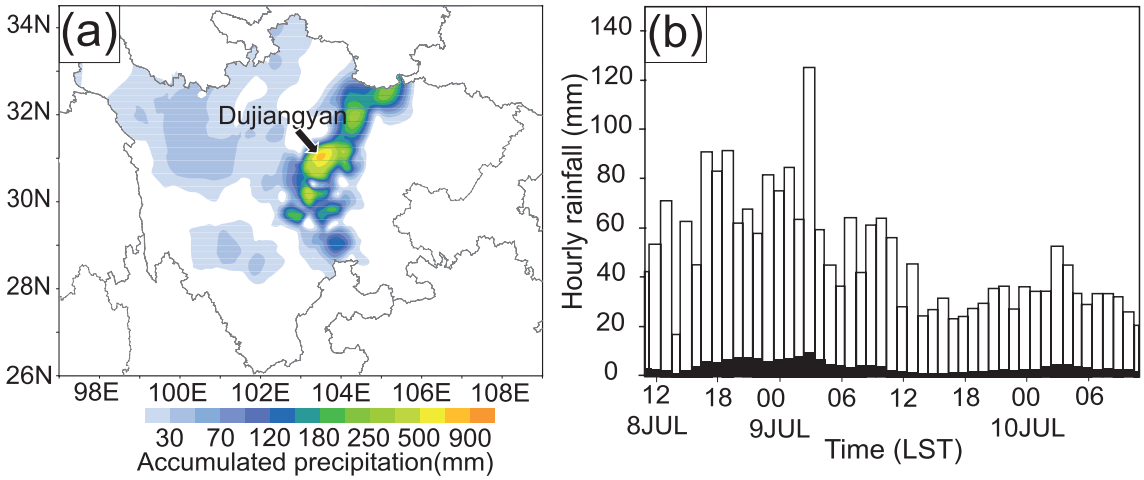

Fig. 1. (a) Observed accumulated precipitation in Sichuan Province during 8–11 July 2013 (color shading; units: mm; "Dujiangyan" denotes the precipitation center of this process). (b) Area extreme hourly rainfall (white bars) and area-averaged hourly rainfall (black bars) (units: mm; computed area covers Sichuan Province) during the period from 1100 LST 8 July to 1100 LST 10 July 2013.

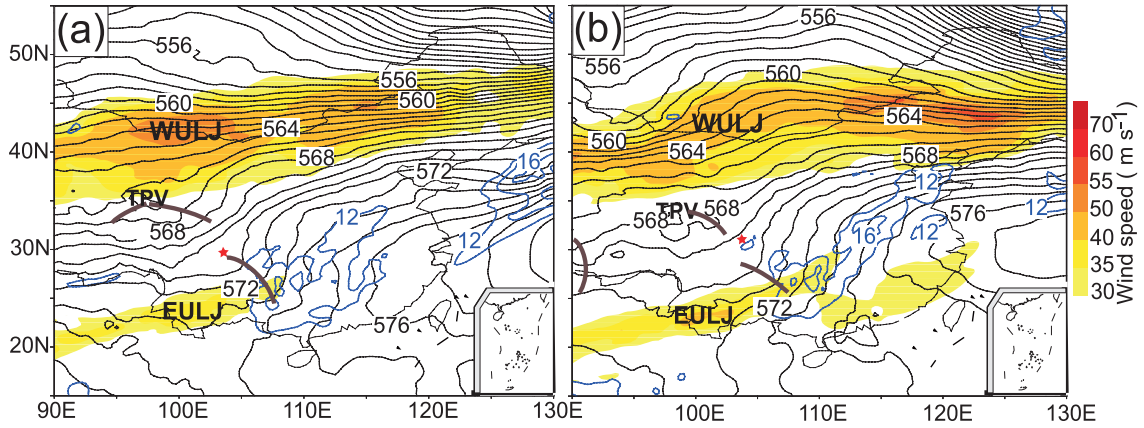

Fig. 2. The 500-hPa geopotential height fields (black contours; units: 10 gpm) superimposed with 200-hPa upper level jet streams (color shading; units: m s^{-1}) and the 850-hPa low level jets (blue contours; units: m s^{-1}), at (a) 2000 LST 8 July 2013 and (b) 2000 LST 9 July 2013. The red star represents the rainfall area; WULJ and EULJ represent the westerly upper-level jet and the easterly upper-level jet, respectively; the brown curves are trough lines.

extended to 115°E. After that, the subtropical high gradually retreated eastward until the second stage of the severe precipitation occurred.

At 200 hPa, the whole precipitation area was controlled by the South Asian High (SAH). Also, two upper-level jet streams moved on the north and south sides of the SAH, forming a sandwich-type pattern together with the precipitation area (Figs. 2a and b). Showing a southwest–northeast orientation, the northern jet stream was a strong westerly jet with relatively stable position and higher intensity. In contrast, the southern one was an easterly jet, weaker and smaller in scale. The low altitude wind below these two upper-level jets sped up to form a north–south low-level jet in the east of the precipitation area after 0800 LST 8 July. Such a configuration of jets and strong precipitation area maintained during the two strong precipitation stages (Fig. 2). Besides the favorable synoptic conditions, both of the two stages of the precipitation process during 8–11 July 2013 were also related to TPVs. Taking the first stage of precipitation (1100 LST 8 July to 1500 LST 9 July) as an example, during that period a cyclonic circulation at 500 hPa and a closed low center at 600 hPa moving from northwest (95°–104°E) to the rainfall area (Figs. 3e–g) were clearly apparent. This vortex was consistent with the characteristics of a typical TPV (Luo, 1992). After it generated, it moved eastward and strengthened. With it moving closer to a Plateau shear line at 700 hPa (Figs. 3a–d), the vorticity and precipitation intensity along the shear line increased. During the early morning on 9 July, when the TPV stagnated around 102°E, a meso-β Southwest Vortex (SWV) (horizontal scale of 100–200 km) was formed on the southern part of the shear line. After sunrise, with the TPV weakening and moving eastward, both the meso-β SWV and precipitation intensity decreased. Such coupling process could also be seen clearly on the isentropic potential vorticity maps [Fig. S1 in the Electronic Supplementary Material (ESM)]. The above analyses suggest that the TPV was one of the key components in producing this severe rainstorm in the middle of Sichuan Province. Therefore, a thorough investigation of this system is needed. In this paper, we explore the relationship between the evolution of the TPV and associated rainfall from the perspective of cloud-top features.

2.2. *Data description*

Besides the conventional surface and radiosonde observations, multispectral satellite observations, including FengYun-2E, Aqua/MODIS, and CALIPSO, and their retrieval products, as well as a high spatiotemporal resolution global reanalysis data from ERA-5, are utilized in this study. Brief descriptions of these data are given as follows:

FengYun-2 is a Chinese second-generation geostationary meteorological satellite. The imager onboard FengYun-2 consists of four infrared channels (centered at 3.75, 6.7, 10.8 and 12.0 μm) and one visible channel with a spatial resolution of 5 km and 1 km, respectively (Xu et al., 2014). The satellite data used in this study are from the FengYun-2E launched at the end of 2008. So far it has been in stable operation. The level-1B dataset of FengYun-2E and its products were acquired from the FengYun Satellite Data Center of the National Satellite Meteorological Center (http://satellite.nsmc.org.cn/portalsite/default.aspx).

MODIS is an important instrument of the Earth Observation System, which aims to observe biological and physical processes at the global scale. It is composed of 36 wave bands (2 bands at 250 m, 5 bands at 500 m, and 29 bands at 1 km) with the spectrum ranging from 0.4 μm to 14.4 μm. In this study, we mainly focus on the characteristics shown in the infrared channel of Aqua/MODIS (band 31, centered at 11.0 μm, spatial resolution of 1 km). The Level-1B dataset (MYD021KM) was obtained from NASA's Atmosphere and Distribution System (http://ladsweb.nascom.nasa.gov). Although the spatial resolution of MODIS is higher compared with geostationary satellite, its temporal resolution is lower (no more than two times a day for the same location). Therefore, MODIS data are used complementally with FengYun-2 geostationary satellite data in this study.

CALIPSO satellite data are also used, to analyze the formation of some cloud-top features from a three-dimensional perspective. CALIPSO is one part of the Aqua satellite constellation (or A-Train), whose mission is to probe the vertical structure and properties of clouds and aerosols over the globe. It consists of three payloads: an active lidar instrument, an imaging infrared radiometer, and a wide field camera. The active lidar instrument, CALIOP, is the key payload on CALIPSO, with a spatial resolution as high as 333 m. It can emit and receive backscatter energy of 532 nm and 1064 nm. Thus, it performs well in detecting cloud particles with small optical depth (Hunt et al., 2009). The L1B dataset (CAL_LID_L1-ValStage1) used in this study was downloaded from NASA's Atmospheric Science Data Center (https://eosweb.larc.nasa.gov/HORDERBIN/HTML_Start.cgi).

In addition to satellite observations, the newest generation of the ECMWF global reanalysis database (ERA-5) is used as a kind of complementary dataset. This dataset has a temporal resolution of 1 h and a horizontal grid spacing of 0.25°. It has 37 vertical layers extending from 1000 hPa near the surface to 0.1 hPa, with a vertical resolution of 25 hPa within the 1000–750 hPa and 250–100 hPa layers. Further details about this dataset can be found at https://www.ecmwf.int/en/forecasts/datasets/reanalysis-datasets/era5.

To evaluate the performance of ERA-5 in reproducing the spatial and temporal distributions of the TPV, a comparison between the cloud cover from ERA-5 and FengYun-2E geostationary observations in the 10.8-μm channel during 2300 LST 8 July to 0800 LST 9 July 2013 is given in Fig. 4. Generally, the synoptic circulations and the spatial and temporal distributions of the TPV cloud cover are captured by ERA-5, indicating that this dataset can be combined with the satellite observations to explore the cloud-top characteristics and their mechanisms related to the TPV in this study.

3. Cloud-top features of the TPV

Cloud can be regarded as the result of interactions between multi-scale dynamic and thermodynamic processes. In

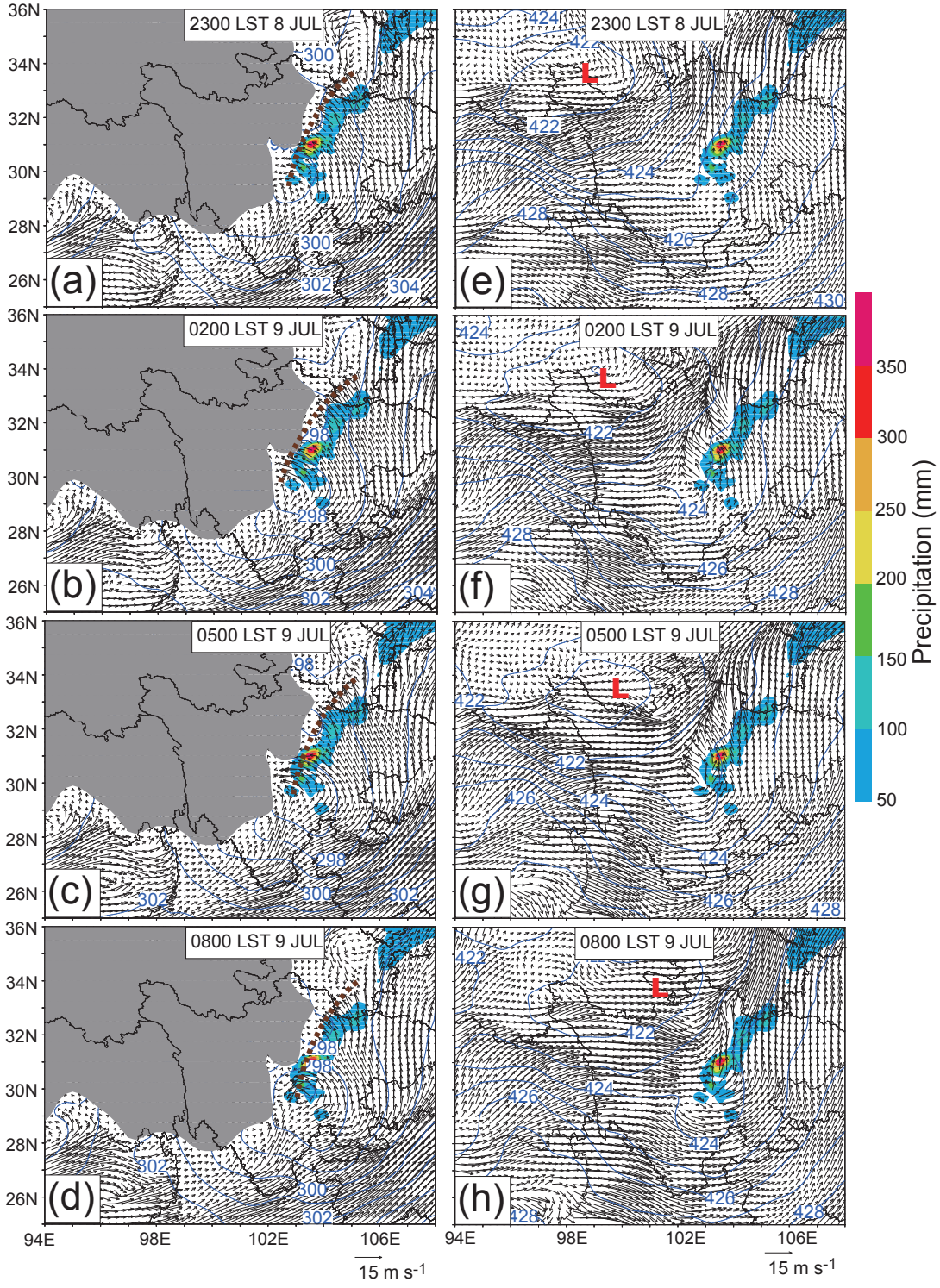

Fig. 3. Time series of circulation (black vectors) and geopotential height (blue contours; units: 10 gpm) at (a) 2300 LST 8 July, (b) 0200 LST 9 July, (c) 0500 LST 9 July, and (d) 0800 LST 9 July, superimposed with accumulated precipitation during 0800 LST 8 to 0800 LST 9 July 2013 (color shading; units: mm). Note that panels (a–d) are for the 700-hPa circulations and geopotential heights, while (e–g) are for the 500-hPa circulations and 600-hPa geopotential heights. The grey shading in (a–d) represents the Tibetan Plateau, and "L" indicates the low-pressure system.

the past several decades, it has been revealed by many studies that some features of convective cloud tops can be used to indicate storm intensity or its inner structure (Purdom, 1976; Adler and Fenn, 1979; Adler et al., 1983). Inspired by these

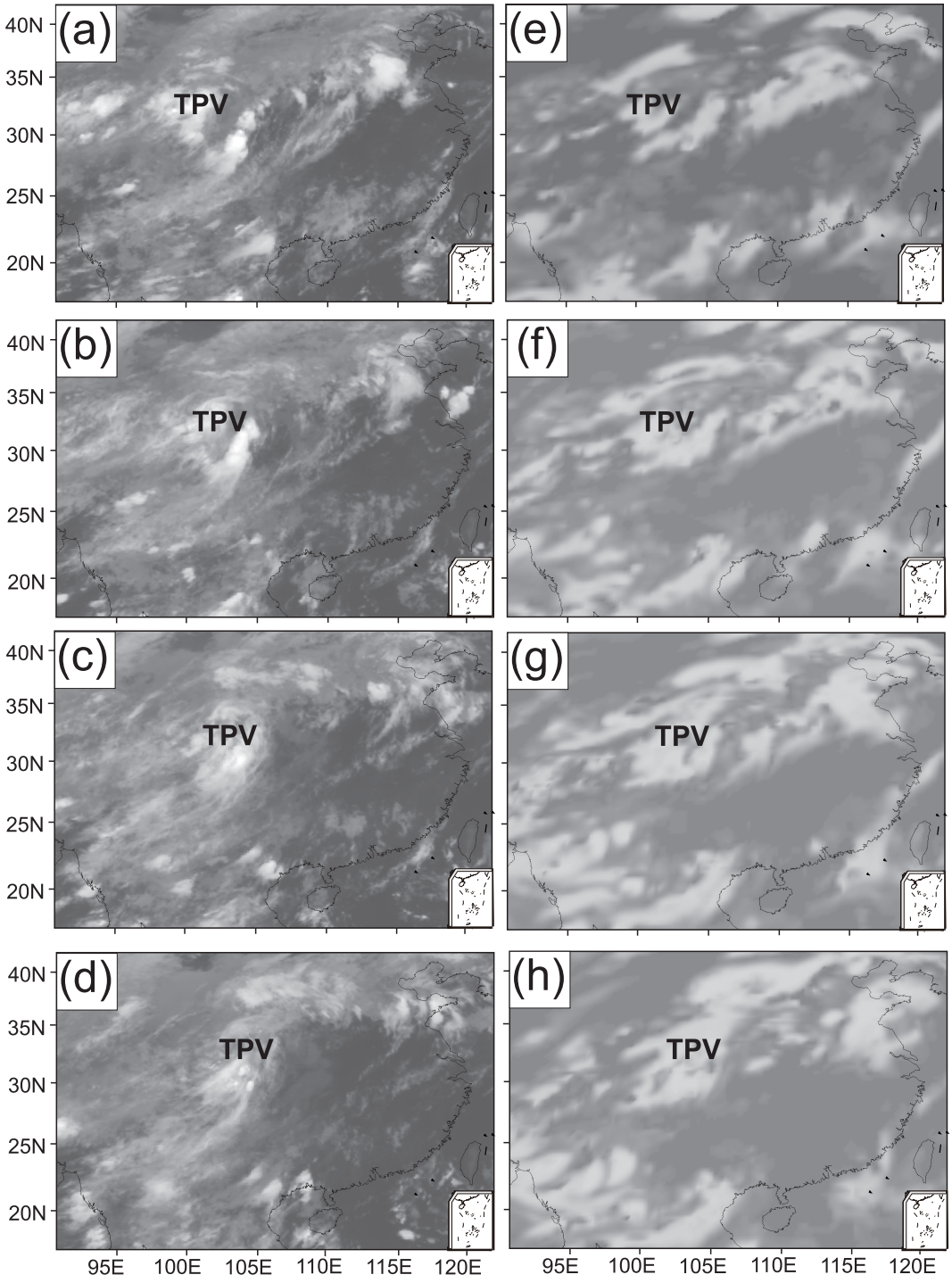

Fig. 4. Comparison between the (a–d) FengYun-2E satellite images and (e–h) ERA-5 high-cloud-cover reanalysis data at (a, e) 2300 LST 8 July, (b, f) 0200 LST 9 July, (c, g) 0500 LST 9 July, and (d, h) 0800 LST 9 July 2013.

studies, cloud-top features of the TPV are explored in detail in this paper.

3.1. *Spatiotemporal characteristics*

Following the automatic cloud-tracking algorithm proposed by Feidas (2003), we first examine the spatiotemporal characteristics of the TPV. In the cloud-tracking algorithm, the size of a TPV is much larger than a meso-β-scale MCS. Therefore, the conditions proposed by Feidas (2003) for meso-β-scale convective system tracking were revised to achieve a consistent and continuous tracking of the TPV. Specifically, in the 10.8-μm infrared channel, the highest TBB was revised from 228 K to 241 K (Maddox, 1983), and the smallest contiguous cloud area was revised from 100 km^2

to 5000 km^2. Compared with the 500-hPa weather map, it is found that, although the TPV was generated around (35°N, 95°E) as early as 1500 LST 8 July (Fig. 3a), it was not until 1700 LST 8 July 2013 that the TPV cloud cluster could be well detected and tracked by using the automatic cloud-tracking algorithm in this study (Fig. 5). This is probably due to the relatively weak convection in the early phase of the TPV and the minimal size of 5000 km^2 we chose for the initial convection detection.

According to the moving tracks shown in Fig. 5a, the TPV first moved to the southeast before 0200 LST 9 July, and then it decelerated and diverted to the northeast. Therefore, the TPV in this case is generally an east-moving vortex with an average moving speed of 12 m s^{-1}. Through the overlay analysis of the moving track and the upper-level wind fields during the same period, it can be seen that the direction of the vortex was consistent with the layer-averaged wind flow within 500–300 hPa, which indicated the TPV was mainly guided by the mid–upper-level flows (Fig. 5a).

For further investigation, the time series of mean TBB in the 10.8-μm infrared channel of FengYun-2E, as well as the relative vorticity and rainfall at 500 hPa within (28°–35°N, 95°–105°E) during 1100 LST 8 July to 1500 LST 9 July are calculated. As suggested by Fig. 5b, there is a strong correlation among the rainfall, TBB and the relative vorticity at 500 hPa. The TBB and rainfall are negatively correlated, with a correlation coefficient of −0.903. The TBB and relative vorticity are also negatively correlated, with a correlation coefficient of −0.82. However, positive correlation exists between the relative vorticity and rainfall, with a correlation coefficient of 0.746. For further comparison, a Hovmöller diagram of the TBB and relative vorticity within the same area during the same period is presented in Fig. 5b, in which the area with TBB lower than 241 K is shaded and superposed onto the positive relative vorticity. One can see that the low-value range of TBB (<241 K), with a fixed horizontal scale of ~500 km, moves from west to east accompanied by a similar-sized relative vorticity maximum area at 500 hPa. These results support our initial hypothesis that the "7.8" severe rainfall is linked to an east-moving TPV, and the cloud features can be quantitatively used to indicate the intensity of the TPV and its associated rainfall.

With respect to the evolution of the TPV, it is found that the precipitation and relative vorticity at 500 hPa started to increase at 1700 LST 8 July, while the TBB started to decrease at the same time. The area-averaged and latitude-averaged TBB (relative vorticity at 500 hPa) dropped below 260 K and 241 K (exceeded 0.5×10^{-5} s^{-1} and 3×10^{-5} s^{-1}), respectively, at 1700 LST 8 July. These obvious changes continued until 2100 LST 8 July, followed by a relative steady state during 2100 LST 8 July to 0600 LST 9 July for all three parameters. After 0600 LST 9 July, opposite changes in the three parameters appeared, compared with the situation before 2100 LST 8 July. Accordingly, the lifespan of the TPV during 8–9 July 2013 could be divided into four stages: initiation (1400–1700 LST 8 July), growth (1700 LST 8 July to 2100 LST 8 July), maturation (2100 LST 8 July to 0600 LST 9 July), and dissipation (after 0600 LST 9 July).

3.2. *Cold-cloud-top areas*

Besides the TBB at the cloud top, the cloud-top morphological features are also used as a monitoring indicator in many statistical forecasting models. DeMaria and Kaplan (1994) and DeMaria et al. (2005) constructed a hurricane intensity forecasting model by using the number of pixels with TBB ⩽ 253 K in four infrared channels of GOES-8, and the

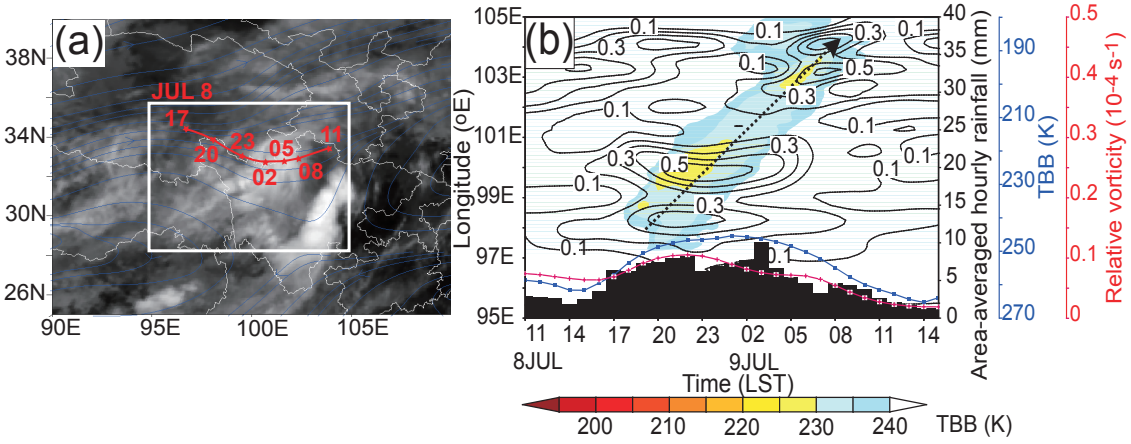

Fig. 5. (a) FengYun-2E 10.8-μm channel satellite image superimposed by the 300–500-hPa layer-averaged flow field (blue flow lines) at 0300 LST 9 July 2013 and the TPV moving track during 1700 LST 8 July to 1100 LST 9 July 2013 (denoted by the red line). The red stars and numbers represent the position and time of the centers of the TPV, respectively. The white frame is the region used for computing the time–longitudinal Hovemöller chart and area-averaged rainfall, TBB and relative vorticity, shown in (b). (b) Time–longitudinal Hovemöller chart of the infrared TBB (color shading for TBB < 241 K; units: K) and positive relative vorticity at 500 hPa (black contours; units: 10^{-4} s^{-1}), along with the time series of the area-averaged hourly TBB, relative vorticity at 500 hPa, and rainfall during 1100 LST 8 July to 1500 LST 9 July 2013 (the dash black arrow indicate the vortex's moving direction).

TBB standard deviation within 100–300 km away from the centers of tropical cyclones, as forecast factors. Fitzpatrick (1997) used the areas of TBB ⩽ 218 K within a 444-km radius of the center of tropical cyclones as an indicator for intensity forecasting.

Inspired by these works, we examine the relationship between the intensity of the TPV and its cold-cloud-top areas. As in section 3.1, the area-averaged relative vorticity is used to indicate the intensity of the TPV. The area used for the calculation is a 5° latitude/longitude area (about 500×500 km^2), taking the center of the TPV as the origin of the coordinates. The cold-cloud-top areas are calculated according to the thresholds developed by Maddox (1983), which are TBB ⩽ 241 K and TBB ⩽ 221 K for convection and deep the convective cloud-top area, respectively. The calculation area is the same as that selected for the relative vorticity calculation. As mentioned in the previous section, during its initiation stage (before 1700 LST 8 July), the TPV cloud clusters were not detected or tracked by the cloud-tracking algorithm used in this paper. Therefore, the centers of the TPV during its initiation were determined by referring to the maximum vorticity at 500 hPa, based on the ERA-5 reanalysis data. In order to facilitate the analysis, the cold-cloud areas are normalized. That is, to calculate the ratio of the areas of cloud temperatures lower than 241 K and 221 K to the total area within a 2.5° radius away from the center of the TPV, which is also referred to as the convective cloud-top area fraction in this study. The computation formulas are shown as follows:

$$\beta_1 = \frac{A_{241}}{A} \tag{1}$$

$$\beta_2 = \frac{A_{221}}{A} \tag{2}$$

Here, A_{241} and A_{221} represent the cold-cloud areas where the TBB is lower than 241 K and 221 K, respectively, and A represents the total area within a 2.5° radius away from the center of the TPV.

As shown by Fig. 6, it is found that both the convective and convective-penetrating cloud-top areas fractions are positively correlated to the intensity of the relative vorticity in the TPV, with correlation coefficients of 0.82 and 0.71, respectively. Also, the changes in these cold-cloud areas were 2–4 hours ahead of the intensity variation of the TPV. Taking the TPV in the growth and dissipation stages for example, the relative vorticity increased (decreased) sharply after 1700 LST 8 July (0600 LST 9 July), while the convective cloud or the convective-penetrating cloud areas notably expanded (reduced) at 1400 LST 8 July and 1500 LST 8 July (0500 LST 9 July and 0200 LST 9 July).

These features reveal that the convective cloud area fraction of the TPV can forecast the variation of TPV intensity. Although both convective and convective-penetrating cloud-top fractions can be used as indicators for TPV objective analysis and forecasting, it seems that the former is more suitable for predicting the growth of a TPV, while the latter for the dissipation of a TPV.

So far, we have identified the potential correlation between cloud-top features and the TPV storm intensity in terms of TBB and cloud-top shape based on mono-channel observations. In the following, we try to find some other meaningful indicators from the multi-spectral channels or multi-sensors of the satellites.

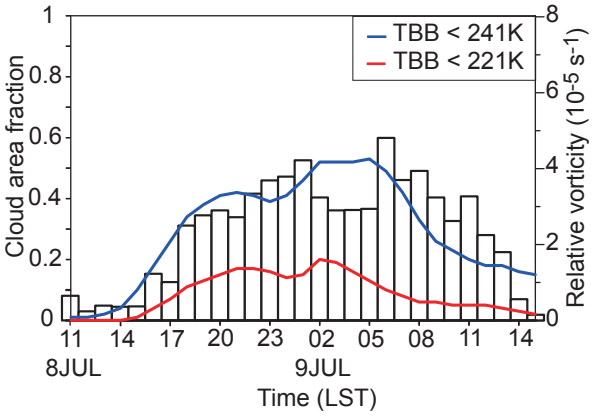

Fig. 6. Time series of the area-averaged relative vorticity at 500 hPa (white bars) and the convective cloud-top area fraction with a threshold of TBB <241 K (blue line) and TBB <221 K (red line) during 1100 LST 8 July to 1500 LST 9 July 2013 (the area used for the computation is within 2.5° latitude/longitude away from the center of the TPV along its moving track).

3.3. *BTDs*

BTDs can provide information on the evolution of cloud-top heights and cloud phases (Lutz et al., 2003). For example, the 6.7-μm (WV channel) and 12-μm infrared channel of the FengYun-2 satellite are sensitive to the upper-level WV, and particle sizes as well as cloud properties, respectively. So, the BTDs between either of them and the 10.8-μm channel are utilized to distinguish between high-level and low-level clouds and gain implicit information about the cloud phases and the optical depths. To be specific, the BTD between the 6.7-μm and 10.8-μm channels is nearly zero when vigorous convection occurs. It can be positive in some parts of the convective system when there is WV in the stratosphere above the cloud top, which is a sign for tropopause-penetrating severe convection. As for the BTD between the 10.8-μm and 12-μm channels, a negative value always indicates a thick ice cloud, and a positive value indicates a thin ice cloud. Figure 7a shows the mean BTDs between the 6.7-μm and 10.8-μm channels, and between the 12-μm and 10.8-μm channels (referred to as $\overline{\Delta T}_{6.7-10.8}$ and $\overline{\Delta T}_{10.8-12}$) within a 2.5° radius away from the center of the TPV. As can be seen, the TPV intensity is positively correlated with the $\overline{\Delta T}_{6.7-10.8}$, but negatively correlated with the $\overline{\Delta T}_{10.8-12}$. The correlation coefficients are 0.82 and −0.68, respectively. These results suggest that the evolutions of the cloud-top microphysics and heights are highly correlated with the vortex intensity.

Besides the WV channel (6.7 μm) and 12-μm infrared channel, the 3.7-μm channel of the FengYun-2 satellite, a mid-wave infrared channel, can also provide useful information on cloud phases and particle sizes. Unlike longwave in-

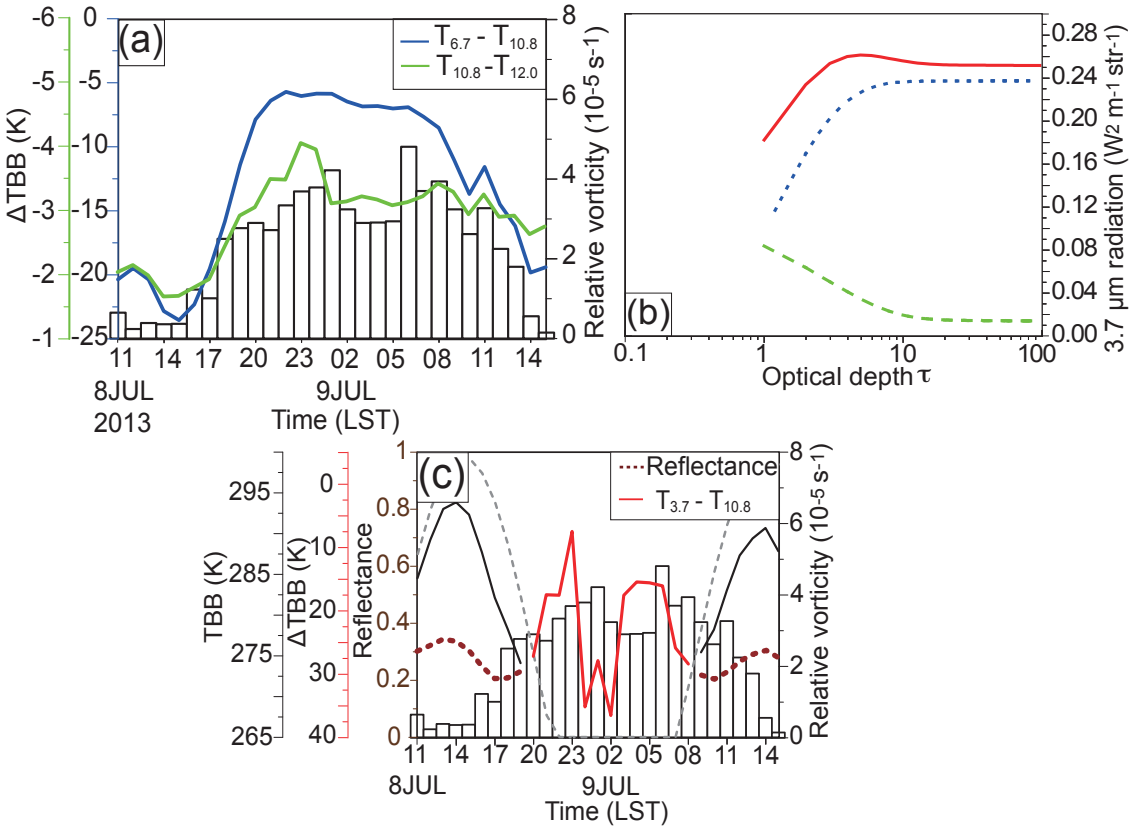

Fig. 7. (a) Time series of the area-averaged relative vorticity at 500 hPa (white bars; units: 10^{-5} s^{-1}), and the BTDs between 6.7 μm and 10.8 μm (blue line; units: K), and between 10.8 μm and 12.0 μm (green line). (b) DSORT-simulated total radiation (red line), emissive radiation (blue dashed line) and reflective radiation (green dashed line) of FengYun-2E at 3.7 μm (solar zenith angle Φ = 50°). (c) Time series of the area-averaged relative vorticity at 500 hPa (white bars; units: 10^{-5} s^{-1}), averaged reflectance (dashed brown line), TBB (black line) during daytime (solar zenith angle Φ ⩾ 20°, indicated by the sinusoidal of the solar zenith angle shown as a grey dashed line), and BTD between 3.7 μm and 10.8 μm during nighttime (red line; units: K; solar zenith angle Φ < 20°) during 1100 LST 8 July to 1500 LST 9 July 2013 (area for computation is the same as that in Fig. 6).

frared channels, such as 10.8 μm or 12 μm, the total radiation received by the satellite in the 3.7-μm channel during the daytime is highly impacted by solar shortwave radiation. Thus, as shown in Fig. 7b, the total radiative energy in this channel is determined not only by the thermally emitted radiation, but also by the reflection of solar radiation (including direct and scattered radiation). Therefore, the daily cloud properties based on this channel should be explored separately during daytime or at nighttime. For a thick cloud, due to cloud shading, the land–sea surface thermal radiation can often be neglected in the total radiation during daytime. Also, given the relatively small ratio of the cloud-emitted thermal radiation to the reflection counterpart, the total radiation of a thick cloud during daytime approximates to the reflected radiation of cloud on solar radiation (Fig. 7b). In terms of the reflection properties, a water cloud with small water droplets (stratus or stratocumulus cloud) always shows a higher reflectance and TBB than an ice cloud (cirrus or cumulonimbus) over land in the 3.7-μm channel. During nighttime, however, without the impact of solar radiation, there is only the thermal emission radiation in the 3.7-μm channel. In that case, similar to the BTD between the 10.8-μm and 12-μm channels, the BTD between the 3.7-μm and 10.8-μm is often used to indicate the cloud properties, for it is more sensitive to changes in cloud-particle size. Normally, a large positive BTD (over 30) between the 3.7-μm and 10.8-μm channels often indicates a cold, high-level cloud with small ice particles on top (Schmidt et al., 1995).

Given the change of the solar zenith angle, the averaged reflectance during daytime (solar zenith angle ⩾ 20°), along with the BTD between the 3.7-μm and 10.8-μm channels at nighttime (solar zenith angle < 20°), within a 2.5° radius away from the center of the TPV, are calculated and compared with the TPV intensity (Fig. 7c). It can be seen that, before and during the initiation stage (1400–1700 LST 8 July) of the TPV, both the reflectance and TBB are high, suggesting a water cloud phase in most parts of the vortex cloud top during this stage. With a rapid increase in the TPV intensity and cloud height during 1700–2100 LST 8 July, an obvious phase change is observed at the cloud top, where water droplets are frozen into ice crystals. After the convective burst, the TPV entered the mature stage (2100 8 July to 0600 LST 9

July). Although the growth of the TPV cloud height slowed (also indicated by the $\overline{\Delta T}_{6.7-10.8}$ and $\overline{\Delta T}_{10.8-12}$ variations), the particle sizes at the TPV cloud top changed notably. As can be seen from Fig. 7c, the $\overline{\Delta T}_{3.7-10.8}$ varies from 5 K to nearly 35 K during 2300 LST 8 July to 0300 LST 9 July when the rainfall enhanced, suggesting a potential correlation between the increase in small ice particles at the cloud top and precipitation enhancement. According to the conceptual model of cloud seeding for rainfall enhancement proposed by Rosenfeld (Rosenfeld, 1997; Rosenfeld and Lensky, 1998), an increase in small ice particles at the cloud top is related to stronger convective overturning. They may act as cloud seeds, and result in precipitation enhancement. After sunrise, most parts of the TPV cloud top gradually changed from ice to water, corresponding to the weakening of the TPV intensity and associated rainfall.

These results indicate that, in the growth and maturation stages, the TPV cloud top generally presents as a cold, high-level cloud with small ice crystal particles. The diurnal changes in cloud top heights, cloud phases, as well as particle sizes revealed by multi-spectral channels have shown a close correlation with the convection and rainfall development associated with the TPV. From the cloud physical processes and their connection to the atmospheric dynamics and thermodynamics, these indicators can be used in predicating the TPV intensity and the associated rainfall enhancement.

3.4. *Cloud-top structures*

Recently, with improvements in infrared sounding, as well as cloud radar technology, cloud-top structures and their correlations with storms have attracted increasing attention. A cold-ring or a cold-U/V structure on the enhanced infrared cloud images, which used to be called an "Enhanced-V" structure, is one of the most attractive features (Heymsfield et al., 1983; McCann, 1983).

Figure 8 is a schematic diagram of the two types of cloud tops in the enhanced 10.8-μm infrared channel. The cold-ring cloud top presents a concentric structure, with a warm spot in the center (CWS in Fig. 8a). The cold-U/V cloud top, however, always shows a semi-circle structure. Two warm areas are usually observed in this case, with one near (close-in warm area; CWA in Fig. 8b), and the other far (distant warm area; DWA in Fig. 8b), from the overshooting tops. Although there are several open questions, such as the formation and maintenance mechanism of these structures, and their indications for the development of weather systems, it is recognized that both structures are related to overshooting tops, and their emergence can be used to indicate storm intensity. As revealed by many previous studies, due to the limited spatiotemporal resolution of observations and the small size and short duration of these structures, the cold-"ring" and cold "U/V" structures can only be found in some mesoscale convective complex cases (Mills and Astling, 1977; McCann, 1983; Setvák et al., 2010, 2013). Nevertheless, scientists believe that these features might appear in many other weather systems with strong convection. To test the hypothesis, in this study, we analyze the TPV cloud-top structures.

Figure 9 shows the Aqua/MODIS band 31 (infrared channel centered at 11 μm) observations of the TPV at 1510 LST 8 July and 0310 LST 9 July, corresponding to its initiation and growth/maturation stages, respectively. Complying with the standard recommended by EUMETSAT's Convection Working Group (https://www.essl.org/cwg/), the TBB in this channel has been color-enhanced. From the figure, we can see that the structures at the TPV cloud top are quite different in the initiation stage and maturation stage. In addition to the prominent increase in the TPV cold-cloud-top heights and areas, another feature is a "U/V"-shaped cold-cloud structure in the northern part of the TPV (denoted as "B" in Fig. 9b). The lowest TBB around the "U/V"-shaped cloud structure

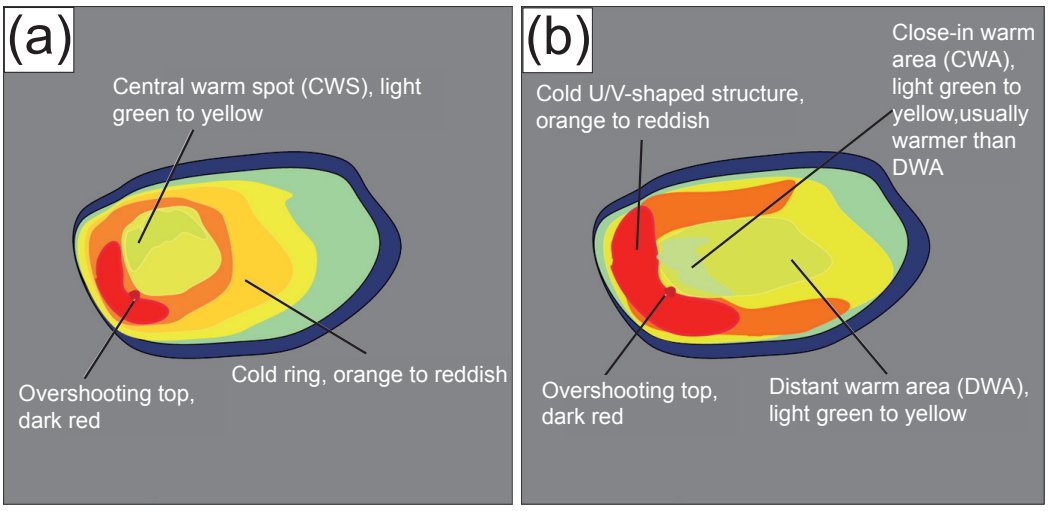

Fig. 8. Schematic illustration of an (a) cold "ring"-shaped cloud top and (b) cold "U/V"-shaped cloud top shown in the color-enhanced 10.8-μm infrared channel (after "Special Investigation: 'Cold Ring' and 'Cold U/V' Shaped storms" http://www.eumetrain.org/satmanu/CMs/Cb/navmenu.php?page=9.0.0). CWS, central warm spot; CWA, close-in warm area; DWA, distant warm area.

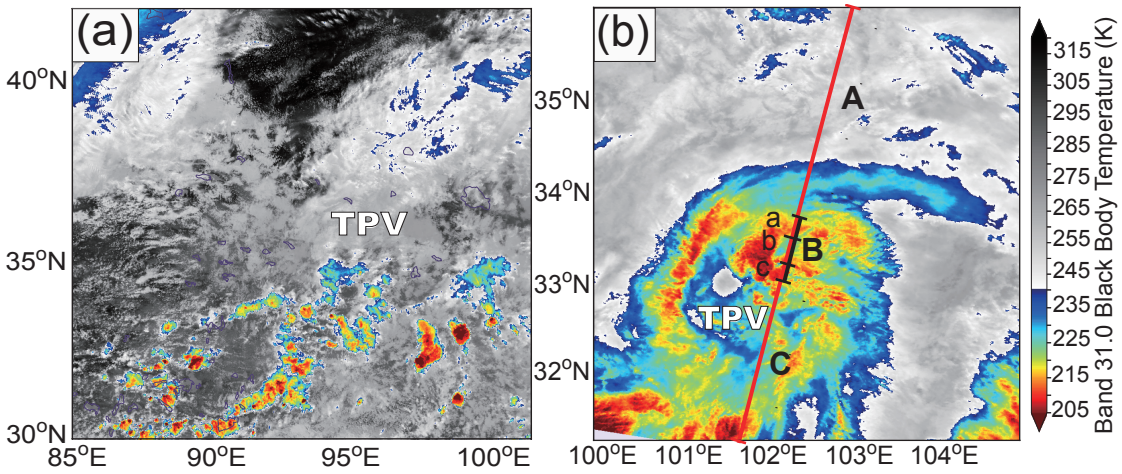

Fig. 9. Color-enhanced Aqua/MODIS channel 31 (centered at 11 μm) cloud images at (a) 1510 LST 8 July 2013 and (b) 0310 LST 9 July 2013. The red line indicates the orbit track of CALIPSO at 0310 LST 9 July 2013; "A", "B" and "C" represent the three different districts of the TPV cloud (the boundary of the three parts is indicated by short red lines along the CALIPSO track); B is the location where the "U/V"-shaped cloud-top structure occurred; "a", "c" and "b", indicated by black lines, correspondingly represent the two cold arms and the circled warm area of the "U/V"-shaped cloud-top structure.

is approximately 200 K (−73°C), and the circled-in highest temperature is about 225 K (−48°C), producing a 25-K BTD within a small region.

Using the same method, the TBB in the 10.8-μm channel of FengYun-2E was also color-enhanced (Fig. 10). As shown in the color-enhanced infrared image observed at 0300 LST 9 July (1900 UTC 8 July), which was almost time-synchronized with the MODIS observation at 0310 LST 9 July (Fig. 9b), a "U/V"-shaped cloud structure (denoted by the black arrow in Fig. 10c) was seen at the same location as that observed in the MODIS band-31 channel. It is estimated that the maximum BTD within this region is about 22 K, which was consistent with that calculated by MODIS observations. According to the time series of the color-enhanced FengYun-2E infrared imagery (Fig. 10), this "U/V"-shaped cloud structure presented as a ring shape 1–2 h before (denoted by the black arrow in Fig. 10b), had an internal–external BTD of about 10 K. Besides the northern part of the TPV, "U/V"-shaped or "ring"-shaped cloud structures were also observed in some other parts of the TPV, especially within the southeastern part of the TPV where upward motion was vigorous. Although both the "U/V"-shaped and the "ring"-shaped structure lasted for a short time, it seems that the "U/V"-shaped structure lived longer than the "ring"-shaped structure in the present case.

4. Discussion

As mentioned above, the formation and maintenance mechanisms of these cloud-top structures are still unclear. Some scientists have suggested that the vertical wind shear is the key factor (Setvák et al., 2010, 2013), while others consider them to be caused by other factors, such as stratosphere–troposphere exchange (Wang, 2007; Wang et al., 2009) or the wake effect (Fujita, 1982; McCann, 1983). The orbits of both Aqua/MODIS and CALIPSO (the orbit track is denoted by the red line in Fig. 9b) passed through the TPV at about 0310 LST 9 July, when a "U/V"-shaped structure occurred, with the CALIPSO obit track crossing its DWA and being vertical to its two cold arms. Figure 11 shows the vertical structure of the total backscatter distribution profile at the wavelength of 532 nm in the "A"–"B"–"C" districts (Fig. 9). The TPV in this case showed a multi-layer structure, with the cloud top up-tilted from north to south and with a maximum height of 17 km. The "B" region in Fig. 11a corresponds to the "U/V"-shaped structure. By zooming in, a fountain-like shape can be seen in the "b" region in Fig. 11b, which corresponds to the warm area of the "U/V"-shaped structure observed by MODIS (Fig. 9b). This fountain-like shape has a maximum height of nearly 15.5 km and a thin feathery cloud above. It is higher than the two cold arms of the "U/V" (denoted as "a" and "c" in Fig. 9b), which are at a height of about 14 km, with the north one covered by a thin feathery cloud.

To further understand its formation, the elements including wind, temperature and moisture, are picked out from the ERA-5 reanalysis data along the obit track of CALIPSO at 0310 LST 9 July. Meanwhile, a diagnostic analysis is made based on these elements (Fig. 12). As shown in Fig. 12, the first remarkable feature is that, in the low level of the cloud, there are several mesoscale positive vorticity columns below the cloud tops whose centers are concentrated within 700–500 hPa (Fig. 12a). The maximum cyclonic vorticity column is under the "U/V"-shaped structure. It also corresponds to a positive abnormal potential vorticity (PV) area (Fig. 12a). According to the PV theory proposed by Hoskins et al. (1985), a positive abnormal PV is closely related to the cyclone column in the lower troposphere. In addition, a positive abnormal PV is also a sign of stratosphere–troposphere exchange. Nor-

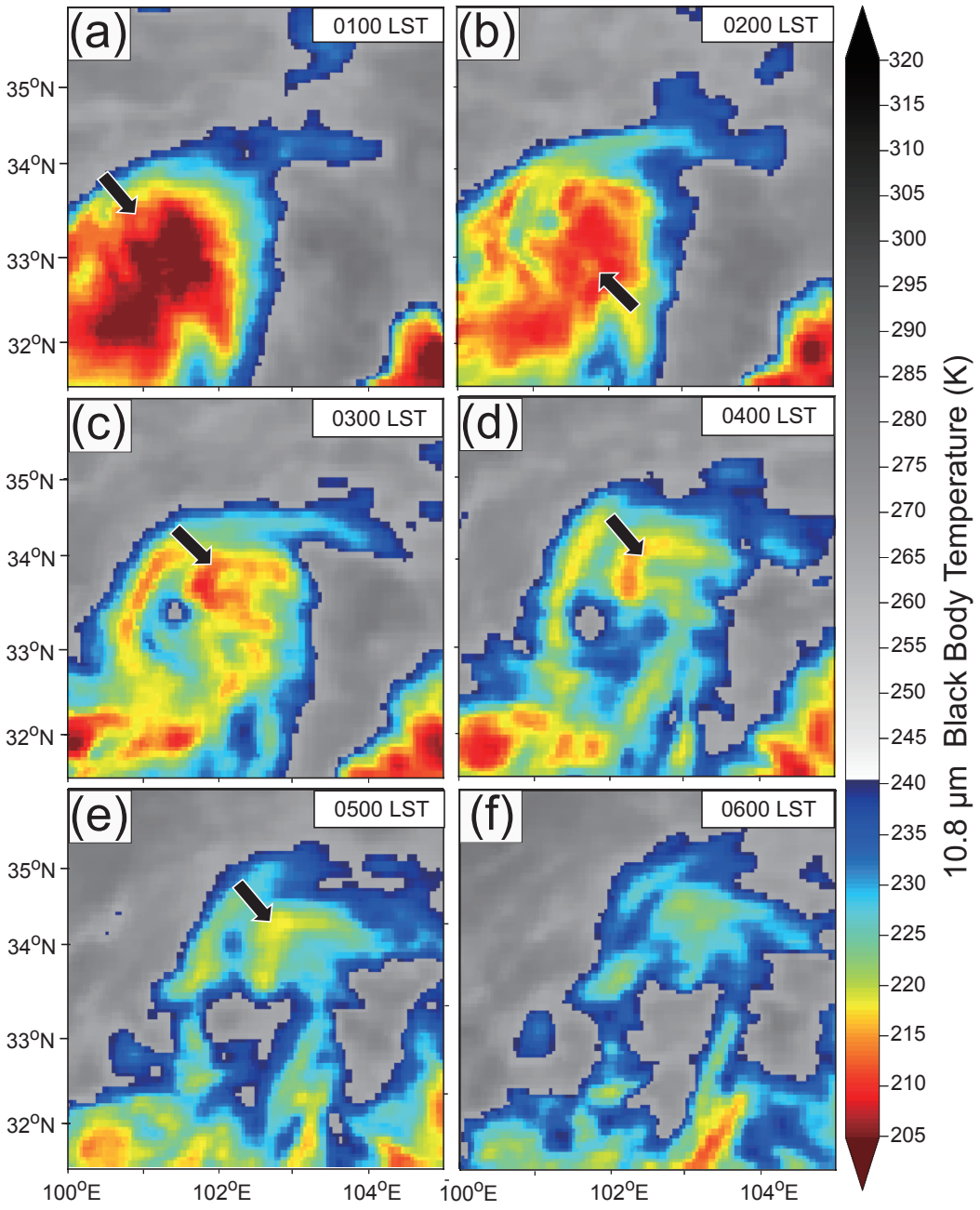

Fig. 10. Color-enhanced FengYun-2E 10.8-μm infrared satellite images during 0100–0600 LST 9 July 2013 (black arrows show the cold-"ring"- or the cold-U/V-shaped cloud structures).

mally, most PVs in the stratosphere are positive, while PVs in the troposphere are likely to be negative. Therefore, the location of 1.5 PVU is used to define the height of the tropopause in most studies. The abnormal PV in this study seems to suggest a tropopause folding or stratospheric intrusion around the "U/V" structure. Due to the significant temperature inversion within the lower stratosphere, pristine ice crystals within the CWA and DWA enter upward into a warmer environment, and then radiate at higher temperatures. Hence, the warmer TBBs appear.

To find out the causes of the tropopause folding or stratospheric intrusion around the "U/V" structure, we examine the formation of this phenomenon from its dynamic field. Two prominent vertical wind shear zones appeared within the TPV cloud cluster: one is at the mid-level of the troposphere within 700–600 hPa; the other is located at the upper level of the troposphere between 300 and 150 hPa. According to the wind field structure (Fig. 12b), the shear zone at the mid-level might be caused by the variations in the wind direction, while the upper-level one is probably related to the variations in wind speed. A jet stream appears around 200 hPa to the north of the "B" region, where the "U/V"-shaped cloud-top structure emerges. As seen in Fig. 2, this area corresponds to the right-hand side of the entrance of the westerly upper-

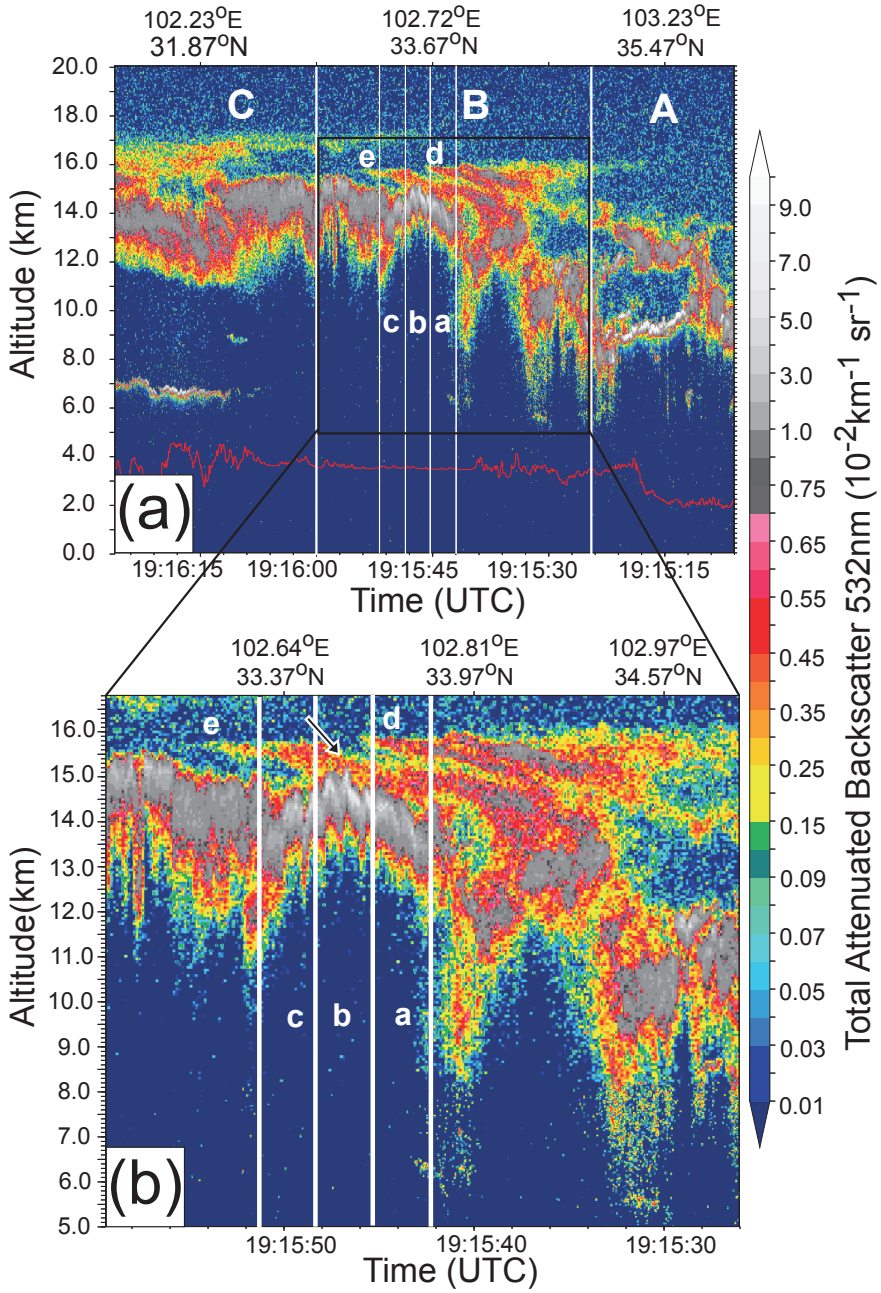

Fig. 11. (a) Vertical cross-section of the total attenuated backscatter (color shading) observed by CALIOP at 532 nm at 0310 LST 9 July 2013, and the (b) enlarged part over "B". "A", "B" and "C", and "a", "b" and "c", correspond to the locations shown in Fig. 9b. The characters "e" and "d" indicate the thin feathery cirrus clouds that occurred over the 'U/V'-shaped cloud top, the black arrow denotes the overshooting top.

level jet (WULJ). As suggested by Zhang and Koch (2000) and Koch et al. (2005), ageostrophic flow is likely to occur in this area, which can induce a gravity wave.

To quantitatively estimate the ageostrophic flow near the TPV in this case, the residual term of the nonlinear balance equation (ΔNBE) (Zhang and Koch, 2000; Zhang, 2004) is used in this study for diagnosis. The mathematical equation is

$$\Delta\mathrm{NBE} = 2\left(\frac{\partial u}{\partial x}\frac{\partial v}{\partial y} - \frac{\partial v}{\partial x}\frac{\partial u}{\partial y}\right) - \nabla^2\Phi + f\zeta - \beta u, \qquad (3)$$

where u, v are the zonal and meridional wind; Φ is the potential height; ∇^2 is the Laplace operator; $\beta = \partial f/\partial y$; and f and ζ represent the geostrophic and relative vorticities, respectively. Usually, a ΔNBE (10^{-8} s^{-2}) with a non-zero value suggests an imbalance in the flow fields (Shou et al., 2003).

As shown in Fig. 12b, the non-zero ΔNBE areas are mainly located in the upper-level troposphere, corresponding to the upper-level vertical wind shear zone with a maximum around the "B" region. This feature supports the theory that the right-hand side of the entrance of a jet stream

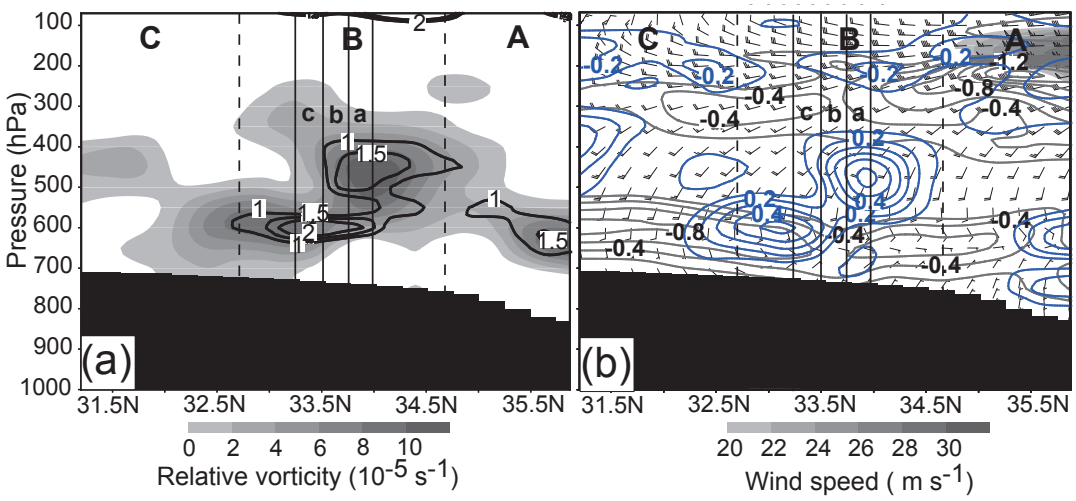

Fig. 12. Vertical distributions of the (a) positive relative vorticity (color shading; units: 10^{-5} s^{-1}) and PV (black solid lines; units: PVU; 1 PVU = 10^{-6} m^2 K s^{-1} kg^{-1}) and (b) strong wind area ($\geqslant$ 20 m s^{-1} shaded), horizontal wind profiles (black wind barbs whereas a full barb is 5 m s^{-1}), vertical wind shear ($\partial|V|/\partial p$; gray lines represent the down-shear area; units: 10^{-2} m s^{-1} pa^{-1}), and the residual term of the nonlinear balance equation ΔNBE (blue lines; units: 10^{-8} s^{-2}) along the CALIPSO obit track at 0310 LST 9 July 2013. Black shading indicates the terrain; "A", "B" and "C", and "a", "b" and "c", as in Fig. 11, correspond to the locations shown in Fig. 9b.

is favorable for inducing ageostrophic flows. Moreover, the large non-zero ΔNBE area around the "B" region also corresponds to the positive abnormal PV region, suggesting a key role played by geostrophic flow in inducing the tropopause folding.

5. Summary

Multispectral data from various low-Earth orbit and geostationary satellites, including FengYun-2E, Aqua/MODIS and CALIPSO, and a high spatiotemporal resolution reanalysis dataset are utilized in this paper. A TPV associated with a severe rainstorm, which occurred in the mid-west of Sichuan Province during 8–11 July 2013, is analyzed. Furthermore, the characteristics of the multi-spectral TBB and TPV cloud top are investigated in detail. Lastly, their correlations with the TPV intensity and inner structural changes are explored. The main conclusions are as follows:

(1) The convective or penetrating-convective cloud area fraction within a 2.5° radius away from the center of the TPV is positively correlated to the TPV intensity. Also, the changes in the cold-cloud-top areas are 2–4 h ahead of the intensity variation. By contrast, the convective cloud-top area fraction (penetrating-convective-cloud area fraction) is much better at indicating the TPV intensification (weakening).

(2) The TPV intensity is also sensitive to the variations in cloud-top phases, optical depth and particle sizes. With the TPV intensification, the TPV cloud top changes from a warm, low-level water cloud to a cold, high-level thick ice cloud, with some parts penetrating the tropopause. Generally, the more intense the TPV is, the thicker and higher the cloud will be. When the TPV is in the maturation stage, the cloud-top height changes are smaller, while the particle size varies notably. It is found that an enhancement of rainfall is accompanied by an increase in small ice crystal particles at the cloud top.

(3) In addition, in the TPV's maturation stage, when it is coupled with an SWV, some cold "U/V"- and "ring"-shaped cloud-top structures are observed in the north and southeast part of the TPV, which are related to the upward motion of the low levels. Considering the formation mechanisms, these structures may be related to tropopause folding, which is partly induced by the intensification of ageostrophic flows. Also, the ageostrophic flows are caused by the vertical wind shear at the upper levels of the troposphere.

Although the present study is based on just one TPV case, some valuable information about the formation and maintenance mechanisms of TPVs can nonetheless be obtained by recognizing the cloud-top features revealed by high spatiotemporal resolution observations. Some findings, such as the correlation between the vortex intensity and the cloud morphological features, the BTDs, and the mechanism of the tropopause folding in inducing the "U/V"-shaped or "ring"-shaped cloud-top structures, are absent in previous TPV studies by means of traditional observations. Moreover, it is found that, although the "U/V"-shaped or "ring"-shaped cloud-top structures can indicate storm severity, they suggest that the cloud infrared temperature and the cloud height may not simply maintain a functional relationship. Therefore, those who construct their forecasting models or make quantitative precipitation estimations simply based on infrared temperature should be aware of this situation. In a forthcoming study, we plan to use a numerical model and more observations, including the new-generation geostationary satellites

FengYun-4 and Himwari-8/9, to determine the quantitative relationship between the cloud-top features and TPV intensity.

Acknowledgements. This research is supported by the National Natural Science Foundation of China (Grant Nos. 41575048 and 91637105). The authors wish to thank Academician Jianmin XU, of the National Satellite Meteorological Center, for giving constructive suggestions during the paper's revision, as well as the anonymous reviewers and editors for their inspirational comments and suggestions on this paper.

Electronic supplementary material. Supplementary material is available in the online version of this article at https://doi.org/10.1007/s00376-018-8049-y.

REFERENCES

Adler, R. F., and D. D. Fenn, 1979: Thunderstorm intensity as determined from satellite data. *J. Appl. Meteor.*, **18**, 502–517, https://doi.org/10.1175/1520-0450(1979)018<0502:TIADFS>2.0.CO;2.

Adler, R. F., M. J. Markusa, D. D. Fennc, G. Szejwacha, and W. E. Shenka, 1983: Thunderstorm top structure observed by aircraft overflights with an infrared radiometer. *J. Climate Appl. Meteor.*, **22**, 579–593, https://doi.org/10.1175/1520-0450(1983)022<0579:TTSOBA>2.0.CO;2.

Bedka, K. M., and J. R. Mecikalski, 2005: Application of satellite-derived atmospheric motion vectors for estimating mesoscale flows. *J. Appl. Meteor.*, **44**, 1761–1772, https://doi.org/10.1175/JAM2264.1.

Chen, G., and G. P. Li, 2014: Dynamic and numerical study of waves in the Tibetan Plateau Vortex. *Adv. Atmos. Sci.*, **31**(1), 131–138, https://doi.org/10.1007/s00376-013-1035-5.

Chen, Z. M., 1988: The dynamic analyses of the effect of large-scale environment flow fields and cumulus on the development of sub-synoptic scale southwest vortex. *Plateau Meteorology*, **7**(1), 27–38. (in Chinese)

Chen, Z. M., M. L. Xu, W. B. Min, and Q. Miao, 2003: Relationship between abnormal activites of Southwest Vortex and heavy rain the upper reach of Yangtze River during Summer of 1998. *Plateau Meteorology*, **22**(2), 162–167, https://doi.org/10.3321/j.issn:1000-0534.2003.02.010. (in Chinese)

Chen, Z. M., W. B. Min, Q Miao, and G. B. He, 2004: A case study on coupling interaction between plateau and southwest vortexes. *Plateau Meteorology*, **23**, 75–80, https://doi.org/10.3321/j.issn:1000-0534.2004.01.011. (in Chinese)

Cheng, X. L., Y. Q. Li, and L. Xu, 2016: An analysis of an extreme rainstorm caused by the interaction of the Tibetan Plateau vortex and the Southwest China vortex from an intensive observation. *Meteor. Atmos. Phys.*, **128**, 373–399, https://doi.org/10.1007/s00703-015-0420-2.

DeMaria, M., and J. Kaplan, 1994: A Statistical hurricane intensity prediction scheme (SHIPS) for the Atlantic Basin. *Wea. Forecasting*, **9**, 209–220, https://doi.org/10.1175/1520-0434(1994)009<0209:ASHIPS>2.0.CO;2.

DeMaria, M., M. Mainelli, L. K. Shay, J. A. Knaff, and J. Kaplan, 2005: Further improvements to the statistical hurricane intensity prediction scheme (SHIPS). *Wea. Forecasting*, **20**, 531–543, https://doi.org/10.1175/WAF862.1.

Feidas, H., 2003: A software tool for monitoring the features of convective cloud systems with the use of Meteosat images. *Environmental Modeling & Software*, **18**, 1–12, https://doi.org/10.1016/S1364-8152(02)00041-5.

Fitzpatrick, P. J., 1997: Understanding and forecasting tropical cyclone intensity change with the Typhoon Intensity Prediction Scheme (TIPS). *Wea. Forecasting*, **12**, 826–846, https://doi.org/10.1175/1520-0434(1997)012<0826:UAFTCI>2.0.CO;2.

Fu, S.-M., W.-L. Li, J.-H. Sun, J.-P. Zhang, and Y.-C. Zhang, 2015: Universal evolution mechanisms and energy conversion characteristics of long-lived mesoscale vortices over the Sichuan Basin. *Atmospheric Science Letters*, **16**, 127–134, https://doi.org/10.1002/asl2.533.

Fujita, T. T., 1982: Principle of stereoscopic height computations and their applications to stratospheric cirrus over severe thunderstorms. *J. Meteor. Soc. Japan*, **60**, 355–368, https://doi.org/10.2151/jmsj1965.60.1_355.

Heymsfield, G. M., G. Szejwach, S. Schotz, and R. H. Blackmer Jr., 1983: Upper-level structure of Oklahoma tornadic storms on 2 May 1979. II: Proposed explanation of "V" pattern and internal warm region in infrared observations. *J. Atmos. Sci.*, **40**, 1756–1767, https://doi.org/10.1175/1520-0469(1983)040<1756:ULSOOT>2.0.CO;2.

Hoskins, B. J., M. E. McIntyre, and A. W. Robertson, 1985: On the use and significance of isentropic potential vorticity maps. *Quart. J. Roy. Meteor. Soc.*, **111**, 877–946, https://doi.org/10.1002/qj.49711147002.

Huang, C. H., and G. P. Li, 2009: A case study of plateau vortex moving east ward with heavy rainfalls based on helicity and non-geostrophic wet *Q*-vector. *Plateau Meteorology*, **28**(2), 319–326. (in Chinese)

Huang, C. H., G. P. Li, J. L. Niu, F. H. Zhao, H. Zhang, and Y. He, 2015: A 30-year climatology of the moving-out Tibetan Plateau vortex in summer and its influence on the rainfall in China. *Journal of Tropical Meteorology*, **31**, 827–838, https://doi.org/10.16032/j.issn.1004-4965.2015.06.011. (in Chinese)

Hunt, W. H., D. M. Winker, M. A. Vaughan, K. A. Powell, P. L. Lucker, and C. Weimer, 2009: *CALIPSO* Lidar description and performance assessment. *J. Atmos. Oceanic Technol.*, **26**, 1214–1228, https://doi.org/10.1175/2009JTECHA1223.1.

Jiang, L. J., and G. P. Li, 2015: Analysis of heavy precipitation caused by the vortices in the lee of the Tibetan Plateau from TRMM (the Tropical Rainfall Measuring Mission) observations. *Proc. Volume 9640, Remote Sensing of Clouds and the Atmosphere XX*, Toulouse, France, SPIE, https://doi.org/10.1117/12.2191821.

Jiang, L. J., G. P. Li, X. T. Wang, 2015: Comparative study based on TRMM data of the heavy rainfall caused by the Tibetan Plateau vortex and the southwest vortex. *Chinese J. Atmos. Sci.*, **39**(2), 249–259, https://doi.org/10.3878/j.issn.1006-9895.1407.13260. (in Chinese)

Koch, S. E., and Coauthors, 2005: Turbulence and gravity waves within an upper-level front. *J. Atmos. Sci.*, **62**, 3885–3908, https://doi.org/10.1175/JAS3574.1.

Kurino, T., 1997: A satellite infrared technique for estimating "deep/shallow" precipitation. *Advances in Space Research*, **19**, 511–514, https://doi.org/10.1016/S0273-1177(97)00063-X.

Li, L., R. H. Zhang, and M. Wen, 2014: Diurnal variation in the occurrence frequency of the Tibetan Plateau vortices. *Meteor. Atmos. Phys.*, **125**, 135–144, https://doi.org/10.1007/s00703-014-0325-5.

Li, L., R. H. Zhang, and M. Wen, 2017: Modulation of the atmospheric quasi-biweekly oscillation on the diurnal variation of the occurrence frequency of the Tibetan Plateau vortices. *Climate Dyn.*, **50**, 4507–4518, https://doi.org/10.1007/s00382-017-3887-3.

Li, J. P., S. G. Wang, and G. W. Sun, 2012: Review and prospects of research on low vortex on the Qinghai-Tibetan plateau. *Journal of Lanzhou University* (*Natural Sciences*), **48**(4), 53–60, 71, https://doi.org/10.3969/j.issn.0455-2059.2012.04.009. (in Chinese).

Lu, J. H., 1986: *The Introduction of Southwest Vortex*. China Meteorological Press, 276 pp. (in Chinese)

Luo, S., 1992: *The Researches of Several Synoptic Systems of Tibetan Plateau and Nearby Areas.* China Meteorological Press, 205 pp. (in Chinese)

Lutz, H.-J., T. Inoue, and J. Schmetz, 2003: Comparison of a split-window and a multi-spectral cloud classification for MODIS observations. *J. Meteor. Soc. Japan*, **81**, 623–631, https://doi.org/10.2151/jmsj.81.623.

Machado, L. A. T., W. B. Rossow, R. L. Guedes, and A. W. Walker, 1998: Life cycle variations of mesoscale convective systems over the Americas. *Mon. Wea. Rev.*, **126**, 1630–1654, https://doi.org/10.1175/1520-0493(1998)126<1630:LCVOMC>2.0.CO;2.

Maddox, R., 1983: Large-scale meteorological conditions associated with midlatitude, mesoscale convective complexes. *Mon. Wea. Rev.*, **111**, 1475–1493, https://doi.org/10.1175/1520-0493(1983)111<1475:LSMCAW>2.0.CO;2.

McCann, D. W., 1983: The enhanced-V: A satellite observable severe storm signature. *Mon. Wea. Rev.*, **111**, 887–894, https://doi.org/10.1175/1520-0493(1983)111<0887:TEVASO>2.0.CO;2.

Mecikalski, J. R., and Coauthors, 2007: Aviation applications for satellite-based observations of cloud properties, convection initiation, in-flight icing, turbulence, and volcanic ash. *Bull. Amer. Meteor. Soc.*, **88**, 1589–1607, https://doi.org/10.1175/BAMS-88-10-1589.

Mecikalski, J. R., K. M. Bedka, S. J. Paech, and L. A. Litten, 2008: A statistical evaluation of GOES cloud-top properties for nowcasting convective initiation. *Mon. Wea. Rev.*, **136**, 4899–4914. https://doi.org/10.1175/2008MWR2352.1.

Mecikalski, J. R., D. Rosenfeld, and A. Manzato, 2016: Evaluation of geostationary satellite observations and the development of a 1–2 h prediction model for future storm intensity. *J. Geophys. Res.*, **121**, 6374–6392, https://doi.org/10.1002/2016JD024768.

Mills, P. B., and E. G. Astling, 1977: Detection of tropopause penetrations by intense convection with GOES enhanced infrared imagery. *Proc. 10th Conf. on Severe Local Storms*, Omaha, Amer. Meteor. Soc., 61–64.

Purdom, J. F. W., 1976: Some uses of high-resolution GOES imagery in the mesoscale forecasting of convection and its behavior. *Mon. Wea. Rev.*, **104**, 1474–1483, https://doi.org/10.1175/1520-0493(1976)104<1474:SUOHRG>2.0.CO;2.

Rosenfeld, D., 1997: Comments on "A new look at the Israeli cloud seeding experiments". *J. Appl. Meteor.*, **36**, 260–271, https://doi.org/10.1175/1520-0450(1997)036<0260:COANLA>2.0.CO;2.

Rosenfeld, D., and I. M. Lensky, 1998: Satellite-based insights into precipitation formation processes in continental and maritime convective clouds. *Bull. Amer. Meteor. Soc.*, **79**, 2457–2476, https://doi.org/10.1175/1520-0477(1998)079<2457:SBIIPF>2.0.CO;2.

Schmetz, J., S. A. Tjemkes, M. Gube, and L. van de Berg, 1997: Monitoring deep convection and convective overshooting with METEOSAT. *Advances in Space Research*, **19**, 433–441, https://doi.org/10.1016/S0273-1177(97)00051-3.

Schmidt, E. O., R. F. Arduini, B. A. Wielicki, R. S. Stone, and S.-C. Tsay, 1995: Considerations for modeling thin cirrus effects via brightness temperature differences. *J. Appl. Meteor.*, **34**, 447–459, https://doi.org/10.1175/1520-0450-34.2.447.

Setvák, M., K. Bedka, D. T. Lindsey, A. Sokol, Z. Charvát, J. Šťástka, and P. K. Wang, 2013: A-Train observations of deep convective storm tops. *Atmos. Res.*, **123**, 229–248, https://doi.org/10.1016/j.atmosres.2012.06.020.

Setvák, M., and Coauthors, 2010: Satellite-observed cold-ring-shaped features atop deep convective clouds. *Atmos. Res.*, **97**, 80–96, https://doi.org/10.1016/j.atmosres.2010.03.009.

Shou, S. W., S. S. Li, and X. P. Yao, 2003: *Mesoscale Meteorology*. China Meteorological Press, 370pp. (in Chinese)

Siewert, C. W., M. Koenig, and J. R. Mecikalski, 2010: Application of Meteosat second generation data towards improving the nowcasting of convective initiation. *Meteor. Appl.*, **17**, 442–451, https://doi.org/10.1002/met.176.

Sun, J. H., J. Li, X. Y. Shen, and L. Kang, 2015: Mesoscale system study of extreme rainfall over Sichuan Basin in July 2013. *Meteorological Monthly*, **41**(5), 533–543, https://doi.org/10.7519/j.issn.1000-0526.2015.05.002. (in Chinese)

Tao, S., 1980: *Rainstorm in China*. Science Press, 225 pp. (in Chinese)

Wang, P. K., 2007: The thermodynamic structure atop a penetrating convective thunderstorm. *Atmospheric Research*, **83**, 254–262, https://doi.org/10.1016/j.atmosres.2005.08.010.

Wang, P. K., M. Setvák, W. Lyons, W. Schmid, and H. M. Lin, 2009: Further evidences of deep convective vertical transport of water vapor through the tropopause. *Atmos. Res.*, **94**, 400–408, https://doi.org/10.1016/j.atmosres.2009.06.018.

Wang, X. F., Y. S. Liao, A. R. Min, and C. G. Cui, 2007: Characteristics of southwest vortex of influencing "05.06.25" Yangtze River rainstorm. *Plateau Meteorology*, **26**(1), 197–205, https://doi.org/10.3321/j.issn:1000-0534.2007.01.023. (in Chinese)

Xiang, S. Y., Y. Q. Li, D. Li, and S. Yang, 2013: An analysis of heavy precipitation caused by a retracing plateau vortex based on TRMM data. *Meteor. Atmos. Phys.*, **122**, 33–45, https://doi.org/10.1007/s00703-013-0269-1.

Xu, J. M., Q. Guo, Q. F. Lu, F. Lu, and X. H. Zhang, 2014: Innovations in the data processing algorithm for Chinese FY meteorological satellites. *Journal of Meteorological Research*, **28**(5), 948–946, https://doi.org/10.1007/s13351-014-4034-2.

Xu, Y. M., H. N. Liu, and G. Y. Xu, 2000: *Introduction of Atmospheric Sciences*. Nanjing University Press, 219 pp. (in Chinese)

Ye, D. Z., and Y. X. Gao, 1979: *Meteorology of the Tibetan Plateau*. Science Press, 316 pp. (in Chinese)

Yu, S. H., 2002: Water vapor imagery of vortex moving process over Qinghai-Xizang Plateau. *Plateau Meteorology*, **21**, 199–204, https://doi.org/10.3321/j.issn:1000-0534.2002.02.013. (in Chinese with English abstract)

Yu, S. H., and G. B. He, 2003: Analysis on application of statellite vapour image to weather prediction over Plateau. *Plateau Meteorology*, **22**, 75–82, https://doi.org/10.3321/j.issn:1000-0534.2003.z1.010. (in Chinese)

Yu, S. H., and W. L. Gao, 2017: Analysis of environmen-

tal background and potential vorticity of different accompanied moving cases of Tibetan Plateau vortex and Southwest China vortex. *Chinese Journal of Atmospheric Sciences*, **41**(4), 831–856, https://doi.org/10.3878/j.issn.1006-9895.1612.16213. (in Chinese)

Yu, S. H., W. L. Gao, J. Peng, and Y. H. Xiao, 2014: Observational facts of sustained departure Plateau Vortexes. *J. Meteor. Res*., **28**(2), 296–307, https://doi.org/10.1007/s13351-014-3023-9.

Zhang, F. Q., 2004: Generation of mesoscale gravity waves in upper-tropospheric jet-front systems. *J. Atmos. Sci*., **61**, 440–457, https://doi.org/10.1175/1520-0469(2004)061<0440:GOMGWI>2.0.CO;2.

Zhang, F. Q., and S. E. Koch, 2000: Numerical simulations of a gravity wave event over CCOPE. Part II: Waves generated by an orographic density current. *Mon. Wea. Rev*., **128**, 2777–2796, https://doi.org/10.1175/1520-0493(2000)128<2777:NSOAGW>2.0.CO;2.

Zhao, Y. C., and Y. H. Wang, 2010: A case study on Plateau vortex inducing southwest vortex and producing extremely heavy rain. *Plateau Meteorology*, **29**(4), 819–831. (in Chinese)

Zhou, K., H. W. Liu, L. Zhao, Y. X. Zhu, Y. H. Lin, F. Y. Zhang, and N. Fu, 2017: Binary mesovortex structure associated with southwest vortex. *Atmospheric Science Letters*, **18**, 246–252, https://doi.org/10.1002/asl.749.

Zhu, F., S. Tao, and L. Chen, 2000: The moist pool over the plateau. *The Second Session of International Workshop on TIPEX (IWTE-I)*, China Meteorological Press, 106–112. (in Chinese)